

Virtual Screening and Crystallographic Studies Reveal an unexpected γ -Lactone Derivative Active against MptpB as a Potential Antitubercular Agent

Giulia Cazzaniga^a, Matteo Mori^a, Fiorella Meneghetti^a, Laurent R. Chiarelli^b, Giovanni Stelitano^b, Isabella Caligiuri^c, Flavio Rizzolio^{c,d}, Samuele Ciceri^a, Giulio Poli^{e,*}, Diana Staver^e, Gabriella Ortore^e, Tiziano Tuccinardi^e, and Stefania Villa^a

^aDepartment of Pharmaceutical Sciences, University of Milan, via L. Mangiagalli 25, 20133 Milano, Italy.

^bDepartment of Biology and Biotechnology "Lazzaro Spallanzani", University of Pavia, via A. Ferrata 9, 27100 Pavia, Italy.

^cPathology Unit, CRO Aviano, National Cancer Institute, IRCCS, Aviano, Italy.

^dDepartment of Molecular Science and Nanosystems, Ca' Foscari University of Venezia, Venezia-Mestre, Italy.

^eDepartment of Pharmacy, University of Pisa, via Bonanno Pisano 6, 56126 Pisa, Italy.

AUTHOR INFORMATION

Corresponding Author

*E-mail: giulio.poli@unipi.it. Phone: +39-050-2219603.

Abstract

Mycobacterial resistance is a rapidly increasing phenomenon requiring the identification of new drugs effective against multidrug-resistant pathogens. The inhibition of protein tyrosine phosphatase B (MptpB), which interferes with host immune responses, may provide a new strategy to fight tuberculosis (TB), while preventing cross-resistance issues. On this basis, starting from a virtual screening (VS) campaign and subsequent structure elucidation studies guided by X-ray analyses, an unexpected γ -lactone derivative (compound **1**) with a significant enzymatic activity against MptpB was identified. The structural characterization of compound **1** was described by means of NMR

spectroscopy, HRMS, single crystal X-ray diffraction and Hirshfeld surface analysis, allowing a detailed conformational investigation. Notably, the HPLC separation of (\pm)-**1** led to the isolation of the most active isomer, which emerged as a very promising MtpB inhibitor, with an IC₅₀ value of 31.1 μ M. Overall, the new chemotype described herein might serve as a basis for the development of novel treatments against TB infections.

Keywords

Mycobacterium tuberculosis, LMW-phosphatases, immune escape mechanisms, tuberculosis, molecular modeling, SC-XRD

ABBREVIATIONS

MtpB, protein tyrosine phosphatase B; TB, tuberculosis; VS, virtual screening; INH, isoniazid; RMP, rifampicin; EMB, ethambutol; PZA, pyrazinamide; MDR/RR-TB, multidrug/rifampicin-resistant tuberculosis; LMW-PTPs, low-molecular weight phosphatases; Mtb, *M. tuberculosis*; PIP, phosphoinositide; TSP, triple-specificity phosphatase; PI3P/PI4P/PI5P, monophosphorylated phosphoinositides; MCV, Mtb-containing vacuole; MD, molecular dynamics; SP, standard precision; XP, extra precision; RMSD, root-mean-square deviation; *p*NPP, *p*-nitrophenyl phosphate; BSA, bovine serum albumin; DTT, 1,4-dithiothreitol; PAIN; pan-assay interference compound; CSD, Cambridge structural database; CCDC, Cambridge Crystallographic Data Centre; HS, Hirshfeld surface; MM-PBSA, Molecular Mechanics - Poisson Boltzmann Surface Area; HTVS, high-throughput virtual screening; GAFF, General Amber force field; TEV, tobacco etch virus

1. Introduction

Despite the global effort to discover innovative anti-tuberculosis (TB) agents, this pathology remains one of the leading causes of death worldwide [1]. In 2019, TB led to 1.4 million deaths, of which 208,000 among HIV-positive patients. The incidence of the pathology decreased by 9% from 2015 to 2019; nevertheless, this decline was too slow to achieve the “End TB Strategy” goal of a 20% reduction in incidence between 2015-2020. Furthermore, due to the COVID-19 pandemic, TB detection in the early 2020 dropped by 50%; consequently, the number of TB deaths is expected to increase to at least 1.8 million [1]. To date, the therapy consists in the co-administration of isoniazid (INH) and rifampicin (RMP) for six months, initially supplemented by two months of ethambutol (EMB) and pyrazinamide (PZA). The resistance to anti-TB drugs is one of the main obstacles to a successful treatment. In 2019, there were an estimated 465,000 incident cases of multidrug- and rifampicin-resistant tuberculosis (MDR/RR-TB), corresponding to 3.3% of all new cases and 17.7% of relapse cases. Most of the resistant strains were insensitive to both RMP and INH (78%); even more worryingly, 20% of MDR-TB cases were resistant to fluoroquinolones, which are commonly used as second-line agents [1]. Furthermore, problems related to the current drugs, such as their toxicity and scarce short-term efficacy, underline the need for new anti-TB drugs acting on innovative targets. In this context, the protein tyrosine phosphatase B (MtpB), one of the two low-molecular weight phosphatases (LMW-PTPs) of *M. tuberculosis* (Mtb) together with MtpA, has been validated as a promising target for the development of innovative anti-TB agents [2–4]. Traditional antibiotics kill Mtb by targeting intra-bacterial functions such as protein, DNA and cell wall biosynthesis. By contrast, MtpB is an extracellular protein, dispensable for *in vitro* growth but essential for *in vivo* viability within the host cell. Selective inhibition of this phosphatase could also increase the intracellular efficacy of first-line antibiotics, like RMP and INH, thus allowing combination therapies. Therefore, due to the extracellular localization of MtpB, the enzymatic inhibitors do not have to cross the bacterial cell wall, which presents a significant challenge for the efficient delivery of

traditional antibacterial agents [2]. Furthermore, MptpB is an attractive and druggable anti-TB target because it is restricted to members of the Mtb complex and shows only a 6% similarity with human phosphatases [5], while MptpA shares 37% of similarity with the human ortholog cytoplasmic protein tyrosine phosphatase HCPTPA [6]. MptpB is secreted by the mycobacterium inside the cytoplasm of macrophages, where it dephosphorylates phosphoserine/threonine, phosphotyrosine, and phosphoinositide (PIP) substrates, thus exhibiting a triple-specificity phosphatase (TSP) activity [5]. The role of MptpB in host cell biology was elucidated by Zhou *et al.* [7]: MptpB interferes with cellular signal transduction pathways activated by IFN- γ , an important inflammatory cytokine, mediating the antimicrobial activity of macrophages. MptpB can attenuate the immune response of the host by decreasing the IFN- γ -stimulated production of IL-6, a key cytokine secreted by the macrophage, which upregulates the microbicidal activity and activates the systemic immune response. MptpB likely blocks IFN- γ -stimulated IL-6 production by downregulating p38 and ERK1/2, two kinases involved in the genetic expression of IL-6. MptpB can also inhibit macrophage apoptosis, a process that is essential to alert the immune system to bacterial invasion. It promotes host cell survival by activating Akt (2.1-fold increase) and blocking caspase 3 activity (2.3-fold reduction) [7]. MptpB dephosphorylates all three monophosphorylated PIPs (PI3P, PI4P, and PI5P), as well as PI(3,5)P₂, depleting PI3P from Mtb-containing vacuoles (MCVs). As PI3P is essential for phagosome-lysosome fusion, the depletion of PI3P arrests the maturation of the vacuoles and facilitates the survival of the *bacilli* in macrophages [8]. In light of these considerations, MptpB constitutes one of the most appealing targets for the development of new anti-TB strategies, and the identification of novel MptpB inhibitors represents a hot topic in medicinal chemistry. In this context, we employed a receptor-based virtual screening (VS) strategy aimed at discovering novel inhibitors of MptpB. Because only a single co-crystal structure of MptpB with an inhibitor, the oxamic acid derivative OMTS (PDB code: 2OZ5) [9], is currently available, this X-ray complex was used as a reference for the VS workflow, in which pharmacophore modeling and screening was combined with a consensus docking protocol and refined by molecular dynamics (MD) simulation studies. The

obtained results led to the disclosure of a novel chemical entity to be developed as alternative and/or complementary therapy for the treatment of TB infections.

2. Results and Discussion

2.1 Virtual Screening

With the aim of identifying novel MptpB inhibitors, we developed a receptor-based virtual screening (VS) study focused on the X-ray structure of MptpB in complex with the inhibitor OMTS (PDB code: 2OZ5) [9], which was used as a reference. By inspecting the X-ray structure, it is possible to note that two OMTS molecules are present in complex with the protein; however, only one molecule is buried within the catalytic site of the enzyme and interacts with the key anchoring residues to which the phosphate ion, a product of the enzymatic reaction, binds [10]. In particular, the oxamic acid moiety of OMTS, well mimicking the product phosphate ion, forms six different H-bonds (Figure 1A). The carboxylic group of the ligand shows three H-bonds with the backbone nitrogen of K164, D165, and R166, as well as an additional interaction with R166 side chain, while the adjacent carbonyl group forms a second H-bond with R166 and another one with the backbone nitrogen of A162. The remaining portions of the inhibitor substantially show hydrophobic interactions with several different residues of the enzyme binding site; most of these involve the chlorobenzyl group of the ligand, which is placed in a big lipophilic pocket delimited by F98, L101, Y125, M126, F161, L199, I203, L227, V231, and L232. The other main lipophilic interactions are observed between P81, H94, F98, and the benzhydryl moiety of the inhibitor.

Based on the various ligand-protein interactions observed in the X-ray complex, we developed a rather minimal receptor-based pharmacophore model, representing only the ligand moieties responsible for the highest number of interactions with the protein, with the aim of pre-filtering a large database of commercial compounds before applying docking-based strategies. For this reason, the generated pharmacophore model contained only four features: three H-bond acceptor features corresponding to the interactions of the carboxylic group of the ligand with the backbone nitrogen of

K164, D165, and R166, identified as key anchoring points, as well as a hydrophobic feature representing the multiple lipophilic interactions established by the benzyl moiety (Figure 1B). The model was refined by adding the exclusion volume spheres, describing the region of space occupied by the protein residues surrounding the ligand, and then used for pre-filtering a database of more than 4 million commercial compounds (see Experimental section for details).

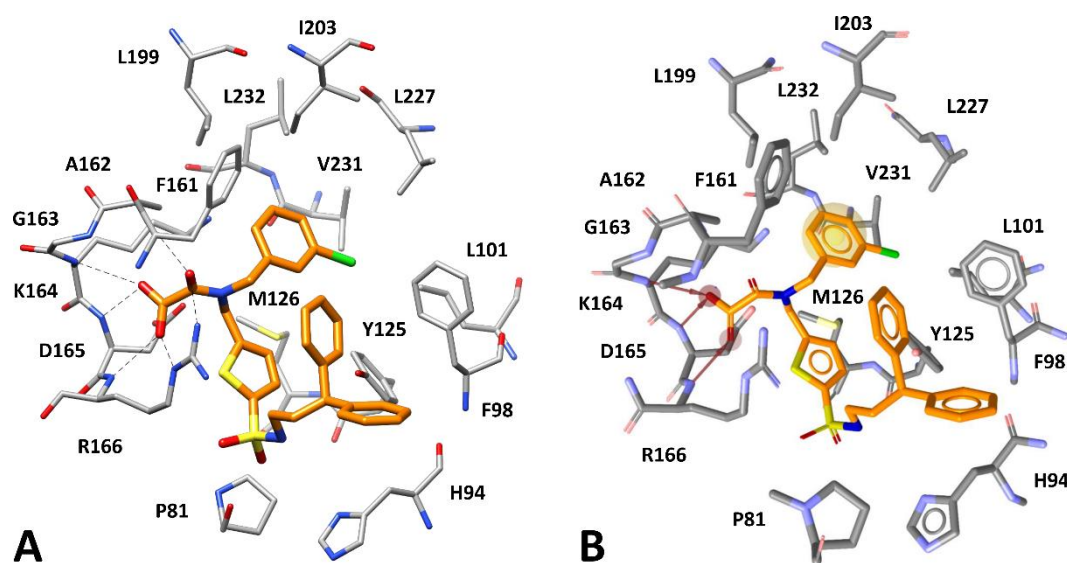


Figure 1. A) Oxamic acid inhibitor OMTS within MptpB binding site (PDB code: 2OZ5). The protein residues surrounding the ligand, shown in orange, are represented as gray sticks, while hydrogen bonds are displayed as dashed lines. B) Receptor-based pharmacophore model with the four different features superimposed to OMTS within MptpB binding site.

By imposing the retrieval of the compounds matching all four pharmacophore features and respecting the volume constraints of the binding site, less than 460,000 molecules were retained. These compounds were then subjected to a fast docking-based filter performed with the use of three H-bond constraints, corresponding to the formation of the key H-bonds with K164, D165, and R166. Specifically, only compounds that could form an energetically favorable binding mode showing the

three H-bonds with K164, D165, and R166 were retained after docking calculations, while the others were automatically discarded. By using this filter, only about 22,400 compounds were selected and further studied through a consensus docking strategy [11]. Specifically, the refined subset of compounds was subjected to a thorough docking-based strategy, in which 13 different docking procedures were employed with the aim of performing a consensus ligand-protein interaction analysis, to identify the compounds most likely to form the expected interactions with the three MptpB key anchoring residues. In this case, no constraint biasing the generation of docking solutions was introduced in any of the 13 docking procedures applied. The consensus docking approach, combining the results of multiple docking methods, has been widely validated by our research group as a strategy able to improve docking reliability with respect to single docking procedures [12]. Moreover, this approach demonstrated to represent a profitable strategy for identifying new hit compounds through VS studies [11]. In fact, within the last decade we reported various VS studies including consensus docking-based protocols that led to the discovery of novel compounds active against different protein targets [13–16]. In this study, with the aim of reducing the computation time due to the use of multiple docking procedures, we adopted a hierarchical two-step consensus docking approach. Initially, the about 22,400 selected compounds were docked into MptpB catalytic site by using six docking procedures, namely Glide with standard precision (SP) and extra precision (XP) methods, Gold with ChemScore and ChemPLP fitness functions, Autodock Vina, and rDock. For each docked compound, the six different binding poses generated by the docking procedures were analyzed in terms of predicted ligand-protein interactions to identify the number of docking solutions in which each ligand was able to form the three key H-bonds with K164, D165, and R166 (see Experimental section for details). After this analysis, only compounds showing the three desired H-bonds in at least two out of the six docking poses were further considered for additional docking studies. Using this approach, about 6,700 ligands were discarded, and less than 15,700 compounds were retained and subjected to the second step of the consensus docking. The retained ligands were docked into the protein binding site with seven additional procedures, i.e., Autodock4, Dock6, Fred,

Gold (with GoldScore and Astex Statistical Potential fitness functions), Glamdock, and Plants, thus generating seven additional poses for each compound. At the end of all docking calculations, the ligand-protein interaction analysis was repeated by taking into account the whole set of 13 solutions (6 + 7) obtained for each ligand from the two steps of the consensus approach. Eventually, only 33 compounds predicted to form the three key H-bonds with K164, D165, and R166 in at least 11 out of the 13 total docking poses were selected for the last evaluation step, based on MD simulations. In detail, the 33 ligand-MptpB complexes generated by the docking experiments were subjected to a 30 ns MD simulation protocol (see Experimental section for details) aimed at assessing the stability of the predicted ligand binding modes and ligand-protein interactions. The results were analyzed in terms of root-mean-square deviation (RMSD) of ligand disposition during the MD, with respect to the initial coordinates, as well as in terms of percentage of H-bond stability during the simulation. Only compounds presenting an average RMSD below 2.0 Å and maintaining at least two out of the three key H-bonds with K164, D165, and R166 for 70% of the whole MD simulation were retained. By using this filter, which represented the last step of our VS workflow (Figure 2), seven compounds were selected to be purchased and subjected to biological evaluation, in order to assess their inhibitory activity (Table 1).

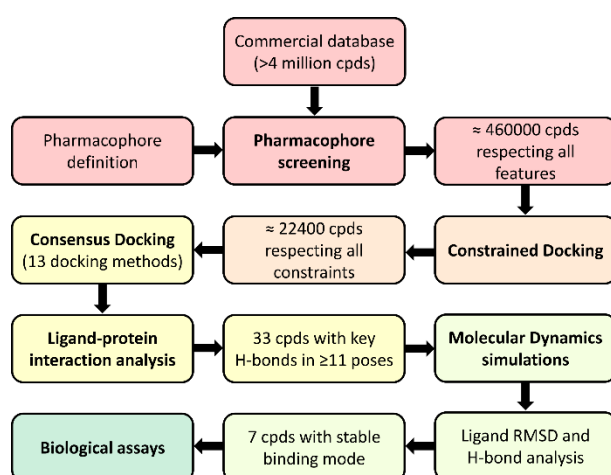


Figure 2. Schematic representation of the virtual screening workflow.

2.2 Biological Evaluation

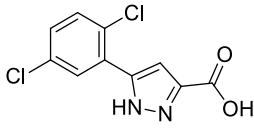
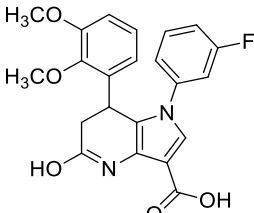
The selected compounds, **1-7**, were tested against MptpB with an assay developed by Chiaradia and co-workers [17], using *p*-nitrophenyl phosphate (*p*NPP) as substrate. The candidate inhibitors were analyzed at a concentration of 100 μ M, and their activity was compared to that of the reference compound **I**, a potent MptpB inhibitor recently disclosed by Vickers and collaborators [18]. Interestingly, four compounds showed an inhibitory effect against MptpB, thus resulting in a hit-rate of about 60%. Among the tested compounds, **1** emerged as the most interesting candidate (Table 1), exhibiting an IC_{50} of $48.1 \pm 2.2 \mu$ M. To validate **1** as a valuable lead MptpB inhibitor, its IC_{50} was re-determined in the presence of bovine serum albumin (BSA, 1 mg/mL) and 1,4-dithiothreitol (DTT, 100 μ M), to prevent the formation of protein aggregates and unspecific interactions with cysteine residues. The retention of the activity (IC_{50} in the presence of BSA: $51.6 \pm 4.2 \mu$ M, and of DTT: $47.0 \pm 2.7 \mu$ M) confirmed that the inhibitor was not a pan-assay interference compound (PAIN) and that its activity was due to its binding to the enzyme (Figure 3A). Finally, in order to preliminary assess the safety profile of compound **1**, the ligand was subjected to antiproliferative assays evaluating its potential cytotoxicity against human fibroblast lung cells MRC5 and WI38 (see Experimental section for details). The compound proved to be inactive against both MRC5 and WI38 cell lines ($IC_{50} > 200 \mu$ M).

Compound **1** was then submitted to further studies, starting from a careful chemical characterization. Alerted by an unexpected 1H NMR spectrum obtained for this compound, we decided to perform a crystallographic investigation to unambiguously determine the structure of **1** (see section 2.4 for details), which was unexpectedly found to be different with respect to that declared by the supplier (Table 1). In detail, the α -keto acid moiety was absent, and, in its place, a γ -lactone connected the quinoline ring to an *o*-substituted phenyl group; moreover, a delocalized π -bond determined the formation of a highly peculiar system between the quinoline and the enol group of the lactone. Considering that a chiral center was present in the experimentally determined structure of **1**, the two

enantiomers, **1-E1** and **1-E2**, were separated and subjected to biological evaluation. Both enantiomers proved to be active on the enzyme (Figure 3B and Table 1), but **1-E1** exhibited a better IC₅₀ value (**1-E1**: IC₅₀ = 31.1 ± 2.7 μM *versus* **1-E2**: IC₅₀ = 72.2 ± 3.4 μM), comparable to that of the reference inhibitor (**I**: IC₅₀ = 25.8 ± 4.5 μM, calculated in the same experimental conditions).

Table 1. *In vitro* activity of **I** and **1-7** against MptpB.

Entry	Structure	%RA at 100 μM	IC ₅₀ (μM)
I (ref.)		10.9 ± 0.7	25.8 ± 4.5
1	 declared by the supplier	24.3 ± 1.1	48.1 ± 2.2
1-E1	-	14.2 ± 1.8	31.1 ± 2.7
1-E2	-	27.7 ± 4.8	72.2 ± 3.4
2		69.5 ± 12.1	n.d. ^a
3		87.2 ± 18.7	n.d. ^a
4		103.7 ± 12.8	n.d. ^a
5		83.2 ± 3.6	n.d. ^a

6		108.9 ± 5.1	n.d. ^a
7		100.9 ± 9.4	n.d. ^a

^aonly determined for compounds with residual activity $\leq 25\%$.

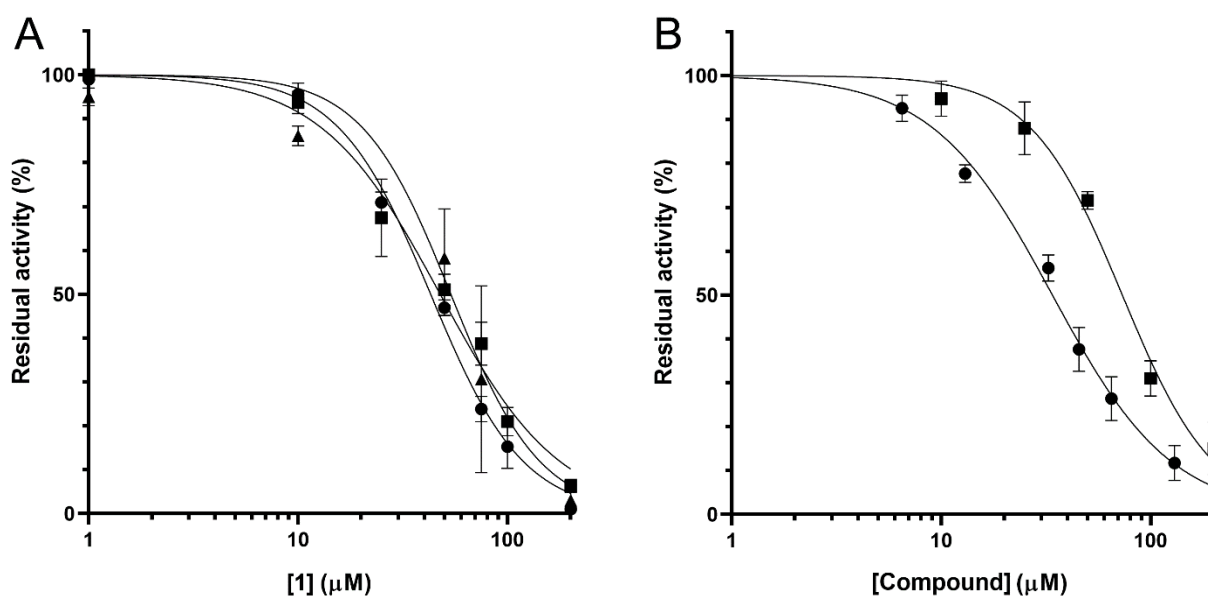


Figure 3. A) Superimposition of the IC_{50} plots of **1** alone (●), and of **1** in the presence of BSA (▲), and DTT (■). B) IC_{50} plot of **1-E1** (●), and **1-E2** (■).

2.3 Chemistry

Compounds **1-7** were purchased at the highest purity grade available (90%) from Enamine (**1,2**; SIA Enamine, Riga, Latvia) and Vitas-M (**3-7**; Vitas M Chemical Ltd., Causeway bay, Hong Kong). The biological assays and analytical tests were performed on the substances as received. The separation of the enantiomeric mixture of **1** was carried out on an HPLC system, using a chiral column. The two components were isolated in high purity and high enantiomeric excess and submitted to the biological tests to measure potential variations in the activity with respect to the mixture. The reference

compound (**1**) was synthesized following a slightly modified literature procedure [18]. In particular, the starting compound 4-bromo-2,6-dichlorophenol was obtained by the bromination of 2,6-dichlorophenol with bromine in acetonitrile. The final compound and all the intermediates were characterized, and the analytical data were consistent with those reported in the literature. More details are available in the Supporting Information.

2.4 Structural Studies on **1**

Crystallographic investigations were performed to unambiguously determine the structure of **1**, the best MptpB inhibitor identified by the VS study and purchased at the highest purity grade available (90%) from the supplier (Enamine). The decision to undertake a deepened molecular characterization was prompted by the unexpected ^1H NMR spectrum of the compound, showing a sharp, intense singlet at 6.81 ppm, which was inconsistent with the proposed structure. The only hydrogen that could have been compatible with the detected signal, *i.e.*, the alkenyl H, was actually expected to be further downfield, at least between 7.5 and 8 ppm. Moreover, the absence of the broad singlet typical of carboxylic acids, even in aprotic solvents (acetone- d_6 and DMSO- d_6), contributed to arouse suspicion on the structure of **1**. This compound crystallized in the orthorhombic space group *Pbca*; its molecular structure is shown in Figure 4 as an ORTEP diagram [19], with an arbitrary atom-numbering scheme.

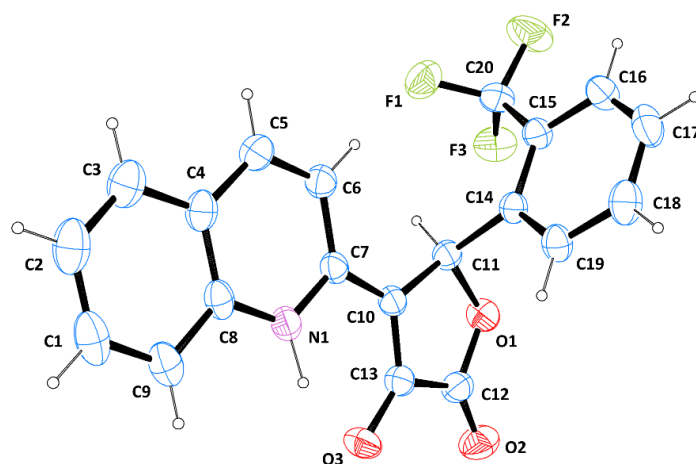


Figure 4. ORTEP diagram of **1**, with the arbitrary atom-numbering scheme. Thermal ellipsoids are set at 30% probability level.

The analysis of the X-ray data revealed an unexpected structure, characterized by the absence of the putative α -ketoacid moiety declared by the supplier. In its place, the quinoline ring proved to be linked to a substituted γ -lactone. The calculation of the bond lengths and angles for the N1-C7-C10-C13-O3 system (Figure 4) indicated a complex electronic configuration, characterized by a significant delocalization of the electron cloud. This peculiar arrangement, which was observed for similar systems in the literature [20,21], can be described in terms of two resonance limit forms in equilibrium (Figure 5), one characterized by an exocyclic double bond (keto-form) and the other by a zwitterion.

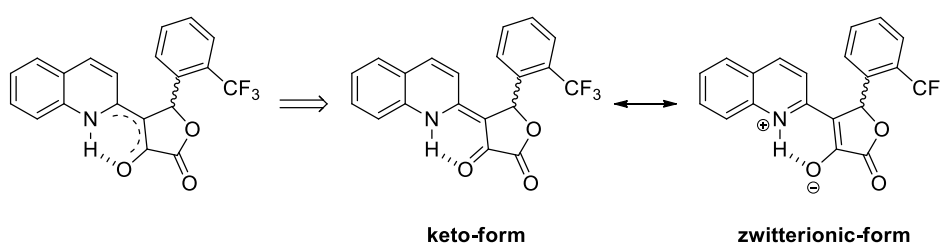


Figure 5. Prototropic tautomerism of **1**, described in terms of its two limit forms.

While previous studies indicated the keto-form as the most stable both in solution and in the solid state, our crystallographic data suggested a shift in the equilibrium towards the zwitterionic form. This determination was based on the N1-C7 and C10-C13 bond lengths, which were 1.343(1) Å and 1.364(1) Å, respectively. Conversely, the lengths of C7-C10 (1.422(1) Å) and C13-O3 (1.291(1) Å) suggested a single-bond character. Anyway, it should be noted that both these values are intermediate between ideal single and double bonds, further confirming the significant conjugation of the system. When the compound was treated as a system with localized bonds, the Mogul program (Cambridge Structural Database, CSD) indicated the C7-C10 bond as highly peculiar, with only a handful of deposited structures sharing this feature (data from Cambridge Crystallographic Data Centre, CCDC). Interestingly, when the structure was analyzed as a delocalized system, the same bond did not trigger any alert. The Mogul analysis also flagged as unusual the N1-C7-C10 (115.9(1)°) and C12-C13-O3 (122.8(1)°) angles; these atypical values are ascribable to the presence of an extremely strong intramolecular H-bond between the charged NH⁺ and O⁻ atoms (D-H = 0.999(1) Å; H...A = 1.799(1)

Å; D⋯A = 2.669(1) Å; D-H⋯A = 143.5(1)°). This interaction is so strong that it alters the overall shape of the system, also impacting on the angle widths. Interestingly, some of the literature hits showing similar angles presented scaffolds that closely resemble that of **1** [21–23]. It is worth mentioning that the solvent may play a role in the distribution of the electronic cloud and that our crystals were grown mainly in a polar protic environment.

Valuable information on the behavior of this system in solution were acquired through the ¹⁵N NMR analysis, which was performed in acetone, a polar aprotic solvent. In detail, the absence of cross-peaks in the ¹H-¹⁵N HSQC experiment and the chemical shift of N-17 (233.2 ppm) suggested the existence of a fast interconversion between the two tautomers of **1** in solution. Interestingly, the experimental chemical shift of N-17 was exactly the average value of the ¹⁵N chemical shifts reported in the literature for 1-phenyl-2-(quinolin-2-yl)ethanone (307.9 ppm; Advanced Chemistry Development Inc., Toronto, ON, Canada) and (Z)-1-phenyl-2-(quinolin-2(1H)-ylidene)ethanone (153.0 ppm) [24].

From the structural point of view, the molecule is composed by three flat portions, represented by the quinoline, the γ-lactone, and the aryl group. The quinoline and lactone rings are almost coplanar, forming an angle of 8.4°, while the phenyl ring is inclined at 85.8° to the best mean-plane of the γ-lactone.

The crystal packing is ensured by π-π stacking interactions between the aromatic portions of the molecule (Figure 6). In detail, the quinoline rings form a parallel-displaced stacking (distance between centroids calculated for the pyridine portion of the quinoline: 3.844 Å; angle between ring normals: 2.3°), while the substituted phenyl group forms a T-shaped stacking with the quinoline (distance between the nearest centroids: 5.627 Å; angle between ring normals: 86.2°). Weak-to-very-weak intermolecular H-bonds between oxygen atoms and aromatic CH contribute to the stabilization of the structure (Figure 6): C5-H5⋯O2 (D-H/Å = 0.930; H⋯A/Å = 2.505; D⋯A/Å = 3.212; D-H⋯A/° = 133.0), C19-H19⋯O3 (D-H/Å = 0.930; H⋯A/Å = 2.489; D⋯A/Å = 3.215; D-H⋯A/° = 135.0), C18-

H18 O1 (D-H/Å = 0.930; H⋯A/Å = 2.725; D⋯A/Å = 3.408; D-H⋯A/° = 131.0), C18-H18 O2 (D-H/Å = 0.930; H⋯A/Å = 2.716; D⋯A/Å = 3.619; D-H⋯A/° = 163.9).

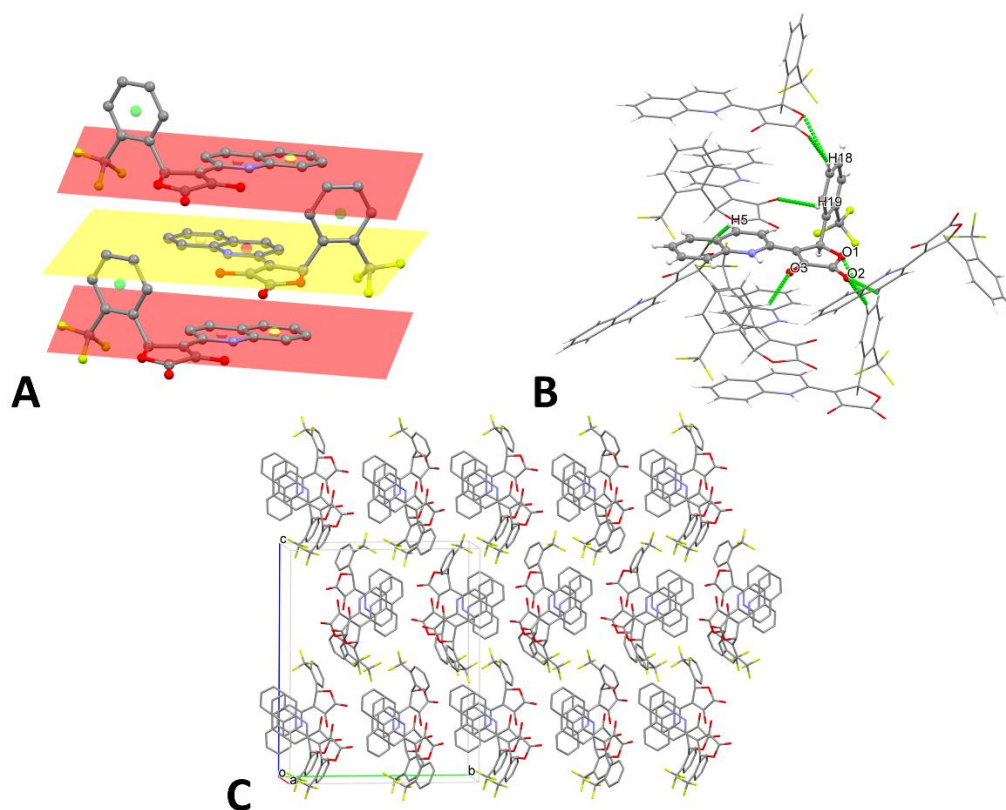


Figure 6. A) Intermolecular π - π stacking interactions; B) intramolecular and intermolecular H-bonds; C) crystal packing viewed along the a axis.

The Hirshfeld surface (HS) of **1** ($V = 403.88 \text{ \AA}^3$, $A = 358.53 \text{ \AA}^2$, $G = 0.737$, $\Omega = 0.145$) was mapped over the normalized contact distance (d_{norm}) and visualized with a red-blue-white color scheme, based on the length of the intermolecular contacts with respect to the sum of the van der Waals radii. As shown in Figure 7A, the surface presents few, and not particularly intense, red regions, corresponding to the weak H-bonds between the O atoms and aromatic CHs. The two-dimensional (2D) fingerprint of the HS confirmed the presence of stacking interactions, as evidenced by the characteristic central green region of the plot (Figure 7B). The formation of weak H-bonds was also demonstrated by the short spikes pointing towards the bottom left corner of the graph. The propensity to form parallel

stacking was further substantiated by the HS mapped over the curvedness, which showed a large flat region, corresponding to the quinoline ring (Figure 7C).

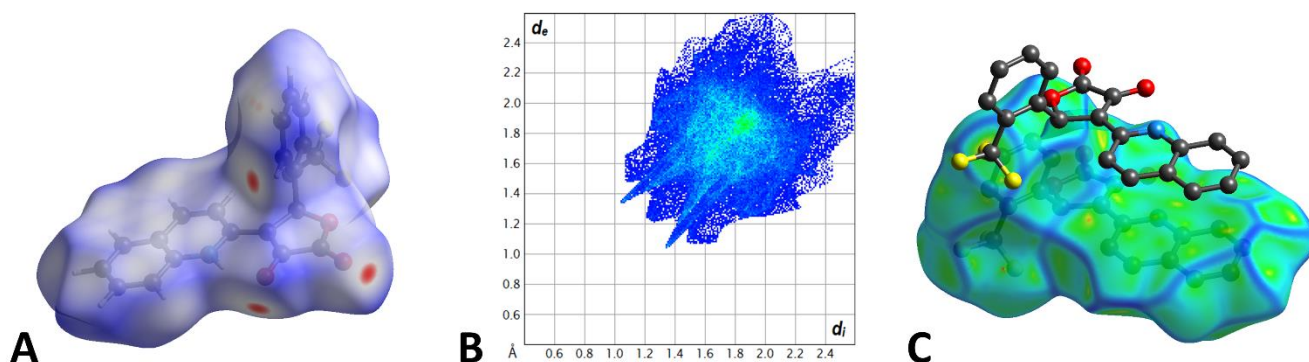


Figure 7. A) Hirshfeld surface of **1** mapped over d_{norm} with a fixed color scale in the range -0.16031 au (red) – 1.4697 au (blue). Red indicates intermolecular contacts shorter than the sum of their van der Waals radii, blue represents contacts longer than the sum of their van der Waals radii, and white marks contacts around the sum of their van der Waals radii. B) 2D Fingerprint plot of **1**, providing a visual summary of the frequency of each combination of d_e and d_i across the HS. Points with a contribution to the surface are colored blue for a small contribution to green for a great contribution. C) HS of **1** mapped over the curvedness (color scale: -4.1060 au – 0.3433 au). Green represents flat regions and blue indicates edges.

Despite the successful separation of the two enantiomers through HPLC, the poor quality of the obtained crystals did not allow for a reliable definition of the absolute configuration through the calculation of the Flack parameter [25]. Furthermore, the lack of available ionizable groups made it impossible to produce salts to favor the determination of the configuration of the stereocenter.

2.5 Molecular Modeling of MptpB-1 Complex

With the aim of predicting a reliable binding disposition for both **1** enantiomers within MptpB binding site, docking and MD simulation studies were performed. Compounds (*S*)-**1** and (*R*)-**1** were docked into MptpB catalytic site by using the 13 docking procedures previously employed within the consensus docking stage of the VS study; the most populated cluster of solutions for each enantiomer

was taken into account and the predicted ligand-protein complex was refined through the same 30 ns MD simulation protocol performed as the last step of the VS workflow. Figure 8 shows the average structures of (*S*)-**1** and (*R*)-**1** within MptpB binding site obtained from the last 15 ns of MD simulation. Notably, both enantiomers were predicted to assume a very stable binding mode (with an average ligand RMSD during the MD around 1.2-1.3 Å) that showed to be consistent with the key ligand-protein interactions observed in the reference X-ray structure and required by the VS protocol. In particular, both compounds share almost the same disposition of the conjugated lactone-quinoline system, essentially differing just for the orientation of the trifluoromethylphenyl ring connected to the chiral center. The central dioxolactone ring of the two enantiomers efficiently mimics the carboxylic group of the reference inhibitor OMTS, forming the three H-bonds with the backbone nitrogen of K164, D165, and R166, which were maintained for most of the MD simulation, as well as a fourth stable H-bond with the guanidine moiety of R166, as observed in the reference X-ray complex. Moreover, the quinoline moiety of both compounds forms an optimal π - π stacking with the side chain of R166 and additional hydrophobic interactions mainly with P81, H94, Y125, and F133. The trifluoromethylphenyl group of (*S*)-**1** and (*R*)-**1** is essentially placed in the big lipophilic pocket delimited by F98, L101, Y125, M126, F161, L199, I203, L227, V231, and L232. However, (*S*)-**1** projects the phenyl ring towards the solvent, which allows the formation of a strong π - π stacking with the side chain of F161 and additional lipophilic interactions with F98, while the trifluoromethyl group mainly interacts with A162, L199, I203, and V231 (Figure 8A). On the contrary, (*R*)-**1** protrudes its phenyl ring within the lipophilic pocket of the binding site, improving the hydrophobic interactions with Y125, M126, and V231, but losing the strong π - π stacking with F161 and the hydrophobic interactions with F98 (Figure 8B). These differences in the ligand-protein interactions predicted for the two enantiomers could be at the basis of their different MptpB inhibitory activity.

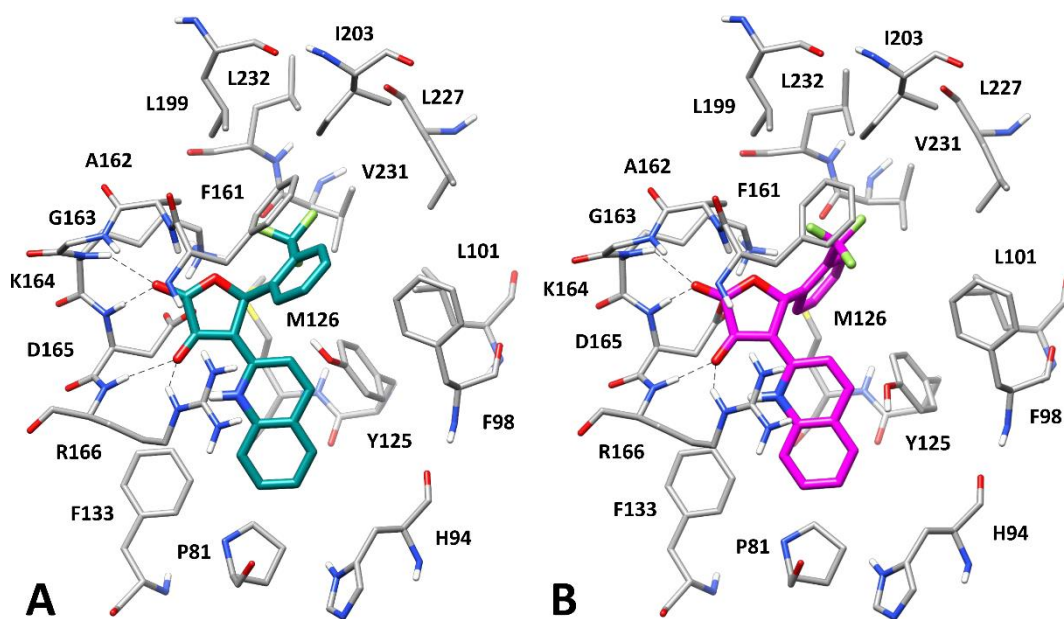


Figure 8. Minimized average structure of (*S*)-**1** (A) and (*R*)-**1** (B) in complex with MptpB. The protein residues surrounding the ligands (dark cyan and magenta, respectively), constituting the binding site, are represented as gray sticks, while hydrogen bonds are showed as black dashed lines.

In order to analyze the binding modes predicted for (*S*)-**1** and (*R*)-**1** from a quantitative point of view, ligand-protein binding free energy evaluations were performed based on the last 15 ns of MD simulation of the two complexes by using the Molecular Mechanics - Poisson Boltzmann Surface Area (MM-PBSA) method (see Experimental section for details) [26]. Because the binding energy calculated for the (*S*)-**1**-MptpB complex (-26.0 kcal/mol) exceeded of about 1.9 kcal/mol that predicted for (*R*)-**1**-MptpB (-24.1 kcal/mol), we might be led to hypothesize that (*S*)-**1** is the eutomer, previously referred to as **1-E1**. However, due to the limited binding energy difference estimated between the two enantiomers, these results substantially confirm that (*S*)-**1** and (*R*)-**1** are both able to bind to MptpB with rather similar affinities, as experimentally observed. Additional experimental studies would be necessary for identifying the absolute configurations of eutomer and distomer of compound **1**.

3. Conclusions

MptpB is a mycobacterial extracellular protein, essential for the *in vivo* viability of Mtb within the host cell. This enzyme shares only about 6% sequence similarity with human phosphatases, thus minimizing the potential risks connected to their inhibition. For these reasons, MptpB represents a new promising target for the development of innovative anti-TB agents. Notably, these novel inhibitors may also increase the intracellular efficacy of first-line antibiotics. In this context, we employed a receptor-based VS protocol, based on the only available MptpB-ligand co-crystal structure, for the identification of new MptpB inhibitors. The VS protocol, combining receptor-based pharmacophore screening with a consensus docking strategy and MD simulations, allowed the identification of four compounds endowed with MptpB inhibitory activity, thus validating the reliability of our *in silico* strategy. Crystallographic studies performed on compound **1**, representing the most promising MptpB inhibitor identified through our VS study, unexpectedly revealed a γ -lactone core moiety bearing a chiral center. The separation of the two enantiomers led to the isolation of the eutomer, which emerged as a very promising MptpB inhibitor, with an IC₅₀ value of 31.1 μ M. Interestingly, **1** shares its characteristic core lactone moiety with a natural MptpB inhibitor extracted from *Aspergillus terreus* SCSIO 41008 [27,28]; this finding contributes to validate this scaffold as a starting point for further developments. Taken together, these results validate the reliability of the VS protocol and highlight the crucial role of crystallographic analyses to unambiguously define the structure of the hit compound, allowing the discovery of a new, unexpected scaffold for the inhibition of MptpB, in the framework of the search for novel anti-TB therapies.

4. Experimental Section

4.1 Pharmacophore Model Generation and Pre-filter

The pharmacophore model was generated using LigandScout 4.2 [29]. The pharmacophore hypothesis was created using the X-ray structure of MptpB in complex with the inhibitor OMTS (PDB code: 2OZ5) [9]. An exhaustive pharmacophore model including all the possible features identified by the program was constructed and, subsequently, only the desired features were retained

in the final pharmacophore model, for a total of 4 features, which included 3 H-bond acceptors and 1 hydrophobic feature. Additionally, the excluded volume spheres, which represent the region of space that could not be occupied by the ligands during the pharmacophore screening, were added to the model. The spheres were automatically defined based on the receptor structure as implemented in the default LigandScout configuration. Approximately 4 million compounds belonging to the Vitas-M, ChemBridge, Enamine, and Pharmeks commercial databases were used as the screening database. The software iCon [30] implemented in LigandScout was used to execute ligand conformational sampling and to set up the screening database. The previously created pharmacophore model, including the excluded volume spheres, was used to pre-filter the generated screening database and to search for compounds with the desired properties. Only the compounds matching all features of the model, which were set as mandatory, were retrieved and considered for further studies.

4.2 Docking Calculations and Consensus Interaction Analysis

All docking calculations were carried out using the X-ray structure of MptpB in complex with the inhibitor OMTS (PDB code: 2OZ5), already used for pharmacophore modeling and screening.

The constrained docking calculations used for refining the pharmacophore-based pre-filter were performed using Glide 5.0 with the high-throughput virtual screening (HTVS) method, as previously described [11,12]. In addition, three different interaction constraints were imposed during the calculations, corresponding to three H-bonds with the backbone N-H groups of K164, D165, and R166. All other settings were left as their defaults. By using these constraints, only compounds for which an energetically favorable binding mode presenting all three H-bonds could be produced were retained after docking calculations, while all others were automatically discarded.

For all other docking calculations, employed in the consensus approach, no constraints were applied. Thirteen different docking procedures were used for this approach: Autodock 4.2.3, Dock 6.7, Fred 3.0, Glide 5.0 with the standard precision (SP) and extra precision (XP) method, GOLD 5.1 (with ChemScore, GoldScore, Astex Statistical Potential, and ChemPLP fitness functions), Autodock Vina

1.1, Glamdock 1.0, Plants, and rDOCK 1.0, employing previously described procedures [11,12]. The analysis of the docking results was performed using the software Binana [31], which allowed the automatic detection of all ligand-protein interactions between each docked compound and MptpB binding site residues. By using an in-house software [32], the interactions detected by Binana for each molecule in each of the 13 docking poses (obtained using the 13 different docking methods) were checked and filtered to identify the number of docking solutions in which the compound showed the three H-bonds with the backbone N-H groups of K164, D165, and R166. After the analysis, a consensus interaction score corresponding to this number was thus assigned to each compound.

4.3 MD Simulations

All simulations were performed using AMBER, version 16. General Amber force field (GAFF) parameters were assigned to the ligands, while partial charges were calculated using the AM1-BCC method as implemented in the Antechamber suite of AMBER 16. The complex was placed in a rectangular parallelepiped water box, by using TIP3P explicit solvent model and solvated with a 15.0 Å water cap. Sodium ions were added as counterions to neutralize the system. Before MD simulations, the whole system was energy-minimized through 5000 steps of steepest descent followed by conjugate gradient, until a convergence of 0.05 kcal/(mol·Å²), imposing a harmonic force constant of 10 kcal/(mol·Å²) only on the protein α carbons. The minimized complexes were used as starting conformations for the MD simulations. PME electrostatics and periodic boundary conditions were used in the simulation. The time step of the simulations was 2.0 fs with a cut-off of 10 Å for the non-bonded interactions; SHAKE was employed to keep all bonds involving hydrogen atoms rigid. A constant volume periodic boundary MD was carried out for 0.5 ns, during which the temperature was raised from 0 to 300 K. The system was then equilibrated through 3 ns of constant pressure simulation, using the Langevin thermostat to maintain the temperature of the system constant. Then, additional 26.5 ns of constant pressure MD production were performed, for a total of 30 ns MD simulation. All the α carbons of the protein were restrained with a harmonic force constant of 10 kcal/(mol·Å²) during

the whole MD simulation. All the obtained MD trajectories were analyzed using the cpptraj program implemented in Amber 16.

4.4 Binding Energy Evaluations

The binding free energy of the MptpB-ligand complexes was calculated with AMBER 16 using the MM-PBSA method [26,33]. The trajectories corresponding to the last 15 ns of MD simulation were used for the evaluation, which was thus performed on a total of 150 MD frames (1 every 100 ps). MOLSURF program and the MM-PBSA module of AMBER 16 were used to calculate nonpolar and polar energies, respectively, while van der Waals, electrostatic, and internal contributions were estimated with the SANDER module. The ligand's entropy was not taken into account in the calculation.

4.5 MptpB Expression, Purification, and Inhibition Assays

The Rv0153c gene, encoding MptpB, was amplified by PCR, using the following primers: forward (5' ATGGGTTCGCGGATCCGAGAATCTTTATTTTCAGGGCATGGCTGTCCGTGAACTGC 3') and reverse (5' TGCGGCCGCAAGCTTTCATCCGAGCAGCACCCC 3'). The primers were designed according to the In-fusion HD Cloning Kit protocol; the forward primer carried the Tobacco etch virus (TEV) protease cleavage site (underlined) to remove the 6-histidine tag from the protein. The purified PCR fragment was recombined into the *Bam*HI-*Hind*III digested pET-28b according to the In-fusion HD Cloning Kit's instructions, to give the pET28b-MPtpB vector. The recombinant products were transformed into *E. coli* StellarTM competent cells, and the resulting colonies were checked for the presence of the insert by colony PCR and sequencing. For the protein expression, *E. coli* BL21(DE3) cells were transformed with pET28b-MptpB and grown in LB medium, containing 50 µg/mL kanamycin, at 37 °C until OD600 = 0.6; then, the culture was induced with 0.5 mM IPTG at 25 °C for 15 h. Cells were harvested by centrifugation, resuspended in 50 mM potassium phosphate buffer pH 8.0, 500 mM KCl, (Buffer A) supplemented with 1 mM phenylmethylsulfonyl fluoride, disrupted by sonication, and centrifuged at 50,000 g for 20 min at 4 °C. The cell-free extract was

loaded on a His-Trap (1 mL; GE Healthcare, Chicago, IL, USA), equilibrated in buffer A; the column was washed with 50 mM imidazole in buffer A, and MptpB eluted with 250 mM imidazole in buffer A. The purified enzyme was dialyzed in 50 mM potassium phosphate pH 8.0, 150 mM KCl (Buffer B), in the presence of 2 mg TEV protease. The digested protein was further purified by a second affinity chromatography, followed by a size exclusion chromatography on a HiLoad Superdex 75 column (GE Healthcare), equilibrated in buffer B. Sample purity was checked by SDS-PAGE, and protein concentration was evaluated according to Lowry [34].

The activity was assayed at 37 °C, using *p*NPP as substrate, and measuring the increase in absorbance at 410 nm due to the formation of *p*-nitrophenol [17]. The standard reaction mixture contained 50 mM Hepes pH 8.0, 100 mM KCl, 1-2 μM MPtpB, and the reactions were initiated by adding 1 mM *p*NPP. Inhibition assays were carried out in the presence of 100 μM of each compound (dissolved in DMSO). Compounds exhibiting more than 70% inhibitory activity at this concentration were further analyzed to determine their IC₅₀, calculated according to the following equation:

$$A_{[I]} = A_{[0]} \times \left(1 - \frac{[I]}{[I] + IC_{50}} \right)$$

where A_[I] is the activity of the enzyme at inhibitor concentration [I] and A_[0] is the activity of the enzyme without the inhibitor.

4.6 PAINS Assay

To exclude pan-assay interference compounds (PAINS), the IC₅₀ plot of **1** was determined as previously described, but in the presence of 0.1 mg/mL BSA to verify the possible formation of aggregates, or in the presence of 100 μM DTT to exclude an inhibition due to covalent reaction with cysteines. The assay was not performed in the presence of Triton X-100 due to interferences of the detergent with the enzymatic assay.

4.7 Chemistry

All starting materials, chemicals, and solvents were purchased from commercial suppliers (Sigma-Aldrich, St. Louis, MI, USA; FluoroChem, Hadfield, UK) and used as received. Anhydrous solvents were utilized without further drying. Aluminum-backed Silica Gel 60 plates (0.2 mm; Merck, Darmstadt, Germany) were used for analytical thin-layer chromatography (TLC), to follow the course of the reactions. Silica gel 60 (40–63 μm ; Merck) was used for the purification of intermediates and final compounds through flash column chromatography. Melting points were determined in open capillary tubes with a Stuart SMP30 Melting Point Apparatus (Cole-Parmer Stuart, Stone, UK). Optical rotatory powers were measured at 23 $^{\circ}\text{C}$ with a Jasco P-1010 polarimeter (Jasco, Easton, MD, USA), using a microcuvette ($l = 0.1$ dm). ^1H NMR spectra of all synthetic intermediates were acquired at ambient temperature with a Varian Oxford 300 MHz instrument (Varian, Palo Alto, CA, USA), operating at 300 MHz for ^1H . As for the tested compounds, NMR spectra were recorded on a Bruker AVANCE 500 spectrometer (Bruker, Billerica, MA, USA), equipped with a 5 mm broadband inverse (BBI) detection probe with field z-gradient operating at 500.13, 125.76, and 50.69 MHz for ^1H , ^{13}C , and ^{15}N , respectively. The spectra were recorded at 298 K in acetone- d_6 (isotopic enrichment 99.9 atom % D). The central peak of acetone- d_6 signals (2.05 ppm for ^1H and 29.84 ppm for ^{13}C spectra, respectively) was used as an internal reference standard. For ^{15}N experiments, nitromethane was used as external reference ($\delta \text{CH}_3\text{NO}_2 = 381.7$ ppm). Data were collected and processed by XWIN-NMR software (version 3.5, Bruker) running on a PC with Microsoft Windows 7. The samples (5 mg) were dissolved in the appropriate solvent (0.75 mL) in a 5 mm NMR tube. The acquisition parameters for 1D were as follows: ^1H spectral width of 5,000 Hz and 32 K data points providing a digital resolution of ca. 0.153 Hz per point, relaxation delay 10 s; ^{13}C spectral width of 29,499 Hz, and 32 K data points providing a digital resolution of ca. 0.900 Hz per point, relaxation delay 2 s. The experimental error in the measured ^1H - ^1H coupling constants was ± 0.5 Hz. The splitting pattern abbreviations are as follows: s, singlet; d, doublet; t, triplet; q, quartet; m, multiplet; and br, broad signal. For two-dimensional experiments, standard Bruker microprograms using gradient selection (gs) were applied. The COSY-45 experiment was acquired with 512 t_1 increments, 2,048 t_2 points, and a spectral width

of 3.0 ppm. Data for HSQC and HMBC experiments were acquired with 512 t_1 increments, 2,048 t_2 points, and a spectral width of 6.0 ppm for ^1H and 200 ppm for ^{13}C . Delay values were optimized to 140 Hz for $^1J_{\text{C,H}}$ and 8.0 Hz for $^nJ_{\text{C,H}}$. The ^1H - ^{15}N HMBC and ^1H - ^{15}N HSQC experiments were performed with an acquisition time of 0.5 s, a relaxation delay between scans of 5 s, a $^1J_{\text{N,H}}$ value of 90.0 Hz, and a $^nJ_{\text{N,H}}$ value of 5.0 Hz. This last parameter was set after several attempts between 1 and 10 Hz. The total experimental time for ^1H - ^{15}N HMBC analysis was 60 hours. ATR-FT-IR spectra were acquired with a Perkin Elmer Spectrum Two FT-IR (Perkin Elmer, Waltham, MA, USA). Tests were performed in a spectral region between 4,000 and 450 cm^{-1} and analyzed by absorbance at a resolution of 4 cm^{-1} after 8 scans. HRMS analyses were carried out on a Q-TOF Synapt G2-Si (Waters Corp., Milford, MA, USA) spectrometer. All spectra and chromatograms can be found in the Supporting Information, along with the analytical characterization of the reference compound **I**.

4.8 Analytical Characterization of 1

Compound **1** was fully characterized by ^1H , ^{13}C , ^{15}N NMR, FT-IR, HRMS, and SCXRD (see Sections 4.10 and 4.11). The NMR study was carried out in acetone- d_6 . Unambiguous assignments of all ^1H , ^{13}C , and ^{15}N signals of the tested compound (Table 2) were established by combining the information gathered from 1D NMR spectra and 2D homocorrelated (COSY) and heterocorrelated (^1H - ^{13}C HSQC, ^1H - ^{13}C HMBC, and ^1H - ^{15}N HMBC) NMR spectra. Most of the proton assignments were accomplished using general knowledge of chemical shift dispersion, with the aid of the proton-proton coupling pattern (^1H NMR spectra) and of the COSY experiment. In ambiguous cases, HSQC and HMBC spectra were used as a definitive and unequivocal tool to make specific assignments. All analytical data are reported below.

mp = 218 °C.

FT-IR (ATR) ν = 3302.30, 3236.27, 2956.23, 2915.20, 2848.65, 1775.94, 1729.45, 1629.34, 1468.98, 1393.43, 1311.84, 1171.18, 1101.07, 1046.35, 979.31, 781.24, 753.28, 719.76, 656.38, 627.21, 522.35, 469.43 cm^{-1} .

ESI-HRMS (m/z) calcd. for $C_{20}H_{13}NO_3F_3$ 372.0848, found 372.0846 $[M+H]^+$; (m/z) calcd. for $C_{20}H_{12}NO_3F_3Na$ 394.0667, found 394.0665 $[M+Na]^+$.

Table 2. 1H , ^{13}C , and ^{15}N NMR data of **1**.

1H NMR (500 MHz, acetone-d_6)		
<i>Atom</i>	<i>1H (ppm)^a</i>	
H-1	7.67 (partially overlapped with H-19 and H-2)	
H-2	7.63 (overlapped with H-19 and H-1)	
H-3	7.58 (d, $J = 7.8$ Hz)	
H-6	7.94 (overlapped with H-18)	
H-7	6.81 (s)	
H-13	6.98 (d, $J = 8.8$ Hz)	
H-14	8.36 (d, $J = 8.8$ Hz)	
H-18	7.94 (overlapped with H-6)	
H-19	7.63 (overlapped with H-1 and H-2)	
H-20	7.87 (ddd, $J = 8.5, 7.0, 1.4$ Hz).	
H-21	8.07 (d, $J = 8.5$ Hz)	
H-28	nd	
^{13}C NMR (126 MHz, acetone-d_6)		
<i>Atom</i>	<i>^{13}C (ppm)^b</i>	<i>HMBC $^{13}C \rightarrow ^1H$</i>
C-1	131.1	H-3
C-2	134.4	H-6
C-3	129.9	H-1 and H-7
C-4	136.3	H-6, H-2, and H-7
C-5	130.2 (q, $J_{C,F} = 30.4$ Hz)	nd
C-6	127.3 (q, $J_{C,F} = 5.8$ Hz)	H-2
C-7	75.0 (m)	H-3
C-8	117.9	H-13 and H-7
C-9	156.0	H-7
C-10	167.7	H-7
C-12	151.5	H-14 and H-13
C-13	119.0	nd
C-14	140.3	H-18
C-15	127.2	H-14, H-21, H-19 and H-13
C-16	143.6	H-14, H-18 and H-20
C-18	129.2	H-14 and H-20
C-19	127.9	H-21
C-20	132.7	H-18
C-21	125.4	H-19
C-24	126.6 (q, $J_{C,F} = 273.4$ Hz)	nd
^{15}N NMR (51 MHz, acetone-d_6)		
<i>Atom</i>	<i>^{15}N (ppm)^c</i>	<i>HMBC $^{15}N \rightarrow ^1H$</i>
N-17	233.2	H-21 and H-13

^a Assignments from 1H - 1H COSY, HSQC, and HMBC data in acetone- d_6 at 298 K. Coupling constants were obtained by direct inspection of the spectra. Experimental error in the measured 1H - 1H coupling constants was ± 0.5 Hz.

^b Assignments from HSQC and HMBC data at 298 K.

^c Assignments from ¹H-¹⁵N HMBC data using nitromethane as the internal reference (δ CH₃NO₂ = 381.7 ppm).

4.9 Enantiomeric separation

The separation of the enantiomeric mixture of **1** was performed on a Merck-Hitachi (Hitachi Ltd., Tokyo, Japan) HPLC unit, equipped with an L-4250 UV-VIS detector, an L-6200 pump system, and a D-2500 chromato-integrator. The following conditions were employed. Column: Phenomenex Lux Cellulose-1 (Phenomenex, Torrance, CA, USA), 250 mm x 4.6 mm, 3 mm. Mobile phase: *n*-hexane/2-propanol 60:40 + 0.1% TFA. Flow rate: 0.5 mL/min. Wavelength: 310 nm. Temperature: 25 °C. A two-step separation procedure yielded the first enantiomer (tR = 19.6 min.) at 97.3% ee and 98.6% purity, and the second enantiomer (tR = 26.0 min) at 99.5% ee and 99.7% purity. The so-obtained stereoisomers were submitted to biological evaluations. The optical rotatory powers were measured on a second batch and are as follows: $[\alpha]_D = -25.0556$ ($c = 0.06$; solvent: MeOH; T = 23 °C; 95% ee) for **1-E1**, and $[\alpha]_D = +27.9394$ ($c = 0.11$; solvent: MeOH; T = 23 °C; 88% ee) for **1-E2**.

4.10 X-ray Crystallography

Crystals of **1** were grown at room temperature by slow evaporation of a 3:1 methanol-chloroform solution. The dark-yellow prisms, which formed reproducibly within 10 days, were analyzed by single-crystal X-ray diffraction. Intensity data were collected on an Enraf-Nonius CAD4 four-circle diffractometer, working at ambient temperature with graphite-monochromatized Mo-K α radiation ($\lambda = 0.7107$ Å). X-ray diffraction data in the 2θ range 4 - 60° and in the (hkl) range +h, +k, \pm l were collected using a profiled ω -scan mode with scan angles of $(1.10 + 0.35 \tan\theta)^\circ$ and prescan speed of 4.12°/min. Accurate unit-cell parameters were obtained by a least-squares fit of the 2θ values for 25 reflections in the 2θ range 16.8 - 28.4°, revealing a metrically orthorhombic unit. The analysis of the systematic absences indicated the space group Pbc_a. Data reductions (including intensity integration, background, Lorentz, and polarization corrections) were performed with the WinGX package

(WinGX v.2014.1) [19]. Absorption effects were evaluated with the psi-scan method and absorption correction was applied to the data (min/max transmission factors were 0.961/0.990). The structure was solved by direct methods using SIR2014 [35] and completed by iterative cycles of full-matrix least squares refinement on F_o^2 and ΔF synthesis using SHELXL-2018/3 [36] within the WinGX suite. Hydrogen atoms were introduced at calculated positions in their described geometries and allowed to ride on the attached atom with fixed isotropic thermal parameters (1.2 U_{eq} of the parent atom for aromatic and methine groups). The structure was analyzed with PARST [37], CSD Mogul [38], and Mercury 2020.2.0 [39]; the graphical representations were rendered with Mercury. Hirshfeld surface analysis was performed with CrystalExplorer 17 [40].

4.11 Crystal Data for 1

Formula: $C_{20}H_{12}F_3NO_3$; MW = 371.31 g/mol; Bravais lattice: orthorhombic; Space group: Pbc_a; Cell dimensions: $a = 7.5510(17)$ Å, $b = 18.8089(18)$ Å, $c = 23.131(4)$ Å; $V = 3285.2(10)$ Å³; $Z = 8$; $D_{calc} = 1.501$ Mg/m³; Crystal size: 0.65 (max), 0.52 (mid), 0.36 (min) mm; $F(000) = 1520$; $T = 293(2)$ K; $2\theta_{min} = 2.166^\circ$; $2\theta_{max} = 25.082^\circ$; Limiting indices = $0 \leq h \leq 9$, $0 \leq k \leq 22$, $-27 \leq l \leq 27$; $R_{int} = 0.0275$; $R = 0.0414$ for 2211 reflections with $F_o > 4\text{sig}(F_o)$ ($R = 0.0578$ for all 2917 unique reflections), $wR2 = 0.0946$ for reflections with $F_o > 4\text{sig}(F_o)$ ($wR2 = 0.1058$ for all unique reflections); $GOOF = 1.077$; Residual positive and negative electron densities in the final map: 0.160 and -0.161 Å⁻³. Full experimental data can be obtained free of charge *via* www.ccdc.cam.ac.uk/conts/retrieving.html (or from the Cambridge Crystallographic Data Centre, 12, Union Road, Cambridge CB21EZ, UK; fax: ++44 1223 336 033; or deposit@ccdc.cam.ac.uk). CCDC entry 2092759 contains supplementary crystallographic data for this paper.

4.12 Cell viability assay. MCR5 and WI38 human fibroblast lung cells (from ATCC) were maintained at 37 °C in a humidified atmosphere containing 5% CO₂ according to the supplier. Cells (10^4) were plated in 96-well culture plates. The day after seeding, vehicle or compound were added at different concentrations to the medium. The compound was added to the cell culture at a concentration ranging

from 200 to 0.02 μM . Cell viability was measured after 96 h according to the supplier (Promega, cat. n° G7571) with a Tecan M1000 PRO instrument, as previously performed [41]. IC_{50} values were calculated from logistical dose response curves. Averages were obtained from two independent experiments, each performed in triplicates.

Declaration of competing interest

The authors declare that they have no known competing financial interests or personal relationships that could have appeared to influence the work reported in this paper.

5. References

- [1] World Health Organization, Global tuberculosis report 2020, Geneva, 2020.
- [2] K.V. Ruddraraju, D. Aggarwal, C. Niu, E.A. Baker, R. Zhang, L. Wu, Z.-Y. Zhang, Highly Potent and Selective N-Aryl Oxamic Acid-Based Inhibitors for Mycobacterium tuberculosis Protein Tyrosine Phosphatase B, *J. Med. Chem.* 63 (2020) 9212–9227.
doi:10.1021/ACS.JMEDCHEM.0C00302.
- [3] K.V. Ruddraraju, D. Aggarwal, Z.-Y. Zhang, Therapeutic Targeting of Protein Tyrosine Phosphatases from Mycobacterium tuberculosis, *Microorganisms*. 9 (2020) 14.
doi:10.3390/microorganisms9010014.
- [4] L. Fanzani, F. Porta, F. Meneghetti, S. Villa, A. Gelain, A. Lucarelli, E. Parisini, Mycobacterium tuberculosis Low Molecular Weight Phosphatases (MPtpA and MPtpB): From Biological Insight to Inhibitors, *Curr. Med. Chem.* 22 (2015) 3110–3132.
doi:10.2174/0929867322666150812150036.
- [5] N. Beresford, S. Patel, J. Armstrong, B. Szöör, A.P. Fordham-Skelton, L. Taberner, MtpB, a virulence factor from Mycobacterium tuberculosis, exhibits triple-specificity phosphatase

activity, *Biochem. J.* 406 (2007) 13–18. doi:10.1042/BJ20070670.

- [6] T. Stehle, S. Sreeramulu, F. Löhr, C. Richter, K. Saxena, H.R.A. Jonker, H. Schwalbe, The Apo-structure of the Low Molecular Weight Protein-tyrosine Phosphatase A (MptpA) from *Mycobacterium tuberculosis* Allows for Better Target-specific Drug Development, *J. Biol. Chem.* 287 (2012) 34569–34582. doi:10.1074/JBC.M112.399261.
- [7] B. Zhou, Y. He, X. Zhang, J. Xu, Y. Luo, Y. Wang, S.G. Franzblau, Z. Yang, R.J. Chan, Y. Liu, J. Zheng, Z.Y. Zhang, Targeting mycobacterium protein tyrosine phosphatase B for antituberculosis agents, *Proc. Natl. Acad. Sci. U. S. A.* 107 (2010) 4573–4578. doi:10.1073/pnas.0909133107.
- [8] H. Hilbi, Modulation of phosphoinositide metabolism by pathogenic bacteria, *Cell. Microbiol.* 8 (2006) 1697–1706. doi:10.1111/j.1462-5822.2006.00793.x.
- [9] C. Grundner, D. Perrin, R.H. van Huijsduijnen, D. Swinnen, J. Gonzalez, C.L. Gee, T.N. Wells, T. Alber, Structural basis for selective inhibition of *Mycobacterium tuberculosis* protein tyrosine phosphatase PtpB, *Structure.* 15 (2007) 499–509. doi:10.1016/J.STR.2007.03.003
- [10] C. Grundner, H.L. Ng, T. Alber, *Mycobacterium tuberculosis* protein tyrosine phosphatase PtpB structure reveals a diverged fold and a buried active site, *Structure.* 13 (2005) 1625–1634. doi:10.1016/j.str.2005.07.017.
- [11] G. Poli, A. Martinelli, T. Tuccinardi, Reliability analysis and optimization of the consensus docking approach for the development of virtual screening studies, *J. Enzyme Inhib. Med. Chem.* 31 (2016) 167–173. doi:10.1080/14756366.2016.1193736.
- [12] T. Tuccinardi, G. Poli, V. Romboli, A. Giordano, A. Martinelli, Extensive consensus docking evaluation for ligand pose prediction and virtual screening studies, *J. Chem. Inf. Model.* 54 (2014) 2980–2986. doi:10.1021/ci500424n.

- [13] G. Poli, N. Giuntini, A. Martinelli, T. Tuccinardi, Application of a FLAP-consensus docking mixed strategy for the identification of new fatty acid amide hydrolase inhibitors, *J. Chem. Inf. Model.* 55 (2015) 667–675. doi:10.1021/ci5006806.
- [14] C. Russo Spena, L. De Stefano, G. Poli, C. Granchi, M. El Boustani, F. Ecça, G. Grassi, M. Grassi, V. Canzonieri, A. Giordano, T. Tuccinardi, I. Caligiuri, F. Rizzolio, Virtual screening identifies a PIN1 inhibitor with possible antiovarian cancer effects, *J. Cell. Physiol.* 234 (2019) 15708–15716. doi:10.1002/jcp.28224.
- [15] M. Lapillo, B. Salis, S. Palazzolo, G. Poli, C. Granchi, F. Minutolo, R. Rotondo, I. Caligiuri, V. Canzonieri, T. Tuccinardi, F. Rizzolio, First-of-its-kind STARD 3 Inhibitor: In Silico Identification and Biological Evaluation as Anticancer Agent, *ACS Med. Chem. Lett.* 10 (2019) 475–480. doi:10.1021/acsmchemlett.8b00509.
- [16] L.R. Chiarelli, M. Mori, D. Barlocco, G. Beretta, A. Gelain, E. Pini, M. Porcino, G. Mori, G. Stelitano, L. Costantino, M. Lapillo, D. Bonanni, G. Poli, T. Tuccinardi, S. Villa, F. Meneghetti, Discovery and development of novel salicylate synthase (MbtI) furanic inhibitors as antitubercular agents, *Eur. J. Med. Chem.* 155 (2018) 754–763. doi:10.1016/j.ejmech.2018.06.033.
- [17] L.D. Chiaradia, P.G.A. Martins, M.N.S. Cordeiro, R.V.C. Guido, G. Ecco, A.D. Andricopulo, R.A. Yunes, J. Vernal, R.J. Nunes, H. Terenzi, Synthesis, Biological Evaluation, And Molecular Modeling of Chalcone Derivatives As Potent Inhibitors of Mycobacterium tuberculosis Protein Tyrosine Phosphatases (PtpA and PtpB), *J. Med. Chem.* 55 (2011) 390–402. doi:10.1021/JM2012062.
- [18] C.F. Vickers, A.P.G. Silva, A. Chakraborty, P. Fernandez, N. Kurepina, C. Saville, Y. Naranjo, M. Pons, L.S. Schnettger, M.G. Gutierrez, S. Park, B.N. Kreiswith, D.S. Perlin, E.J. Thomas, J.S. Cavet, L. Taberner, Structure-Based Design of MptpB Inhibitors That Reduce Multidrug-Resistant Mycobacterium tuberculosis Survival and Infection Burden in Vivo, *J.*

Med. Chem. 61 (2018) 8337–8352. doi:10.1021/ACS.JMEDCHEM.8B00832.

- [19] L.J. Farrugia, WinGX and ORTEP for Windows: An update, *J. Appl. Crystallogr.* 45 (2012) 849–854. doi:10.1107/S0021889812029111.
- [20] R. Dobosz, E. Kolehmainen, A. Valkonen, B. Ośmiałowski, R. Gawinecki, Tautomeric preferences of phthalones and related compounds, *Tetrahedron.* 63 (2007) 9172–9178. doi:10.1016/J.TET.2007.06.064.
- [21] Y.A. Sayapin, B.N. Duong, V.N. Komissarov, I. V. Dorogan, N.I. Makarova, I.O. Bondareva, V. V. Tkachev, G. V. Shilov, S.M. Aldoshin, V.I. Minkin, Synthesis, structure, and photoisomerization of derivatives of 2-(2-quinolyl)-1,3-tropolones prepared by the condensation of 2-methylquinolines with 3,4,5,6-tetrachloro-1,2-benzoquinone, *Tetrahedron.* 66 (2010) 8763–8771. doi:10.1016/J.TET.2010.08.077.
- [22] S.B. Wagh, P. Sharma, M.D. Patil, R.-S. Liu, Gold-catalyzed oxidative cycloalkenations of alkynes with quinoline N -oxides, *Org. Chem. Front.* 6 (2019) 226–230. doi:10.1039/C8QO01175C.
- [23] Z.-S. Chen, F. Yang, H. Ling, M. Li, J.-M. Gao, K. Ji, Metal-Free, Site-Selective Addition to Ynones: An Approach to Synthesize Substituted Quinoline Derivatives, *Org. Lett.* 18 (2016) 5828–5831. doi:10.1021/ACS.ORGLETT.6B02813.
- [24] M. Sakamoto, M. Abe, K. Ishii, Studies on Conjugated Nitriles. VI. Reaction of 2-Methylquinoline and Related Compounds with Acyl Cyanides, *Chem. Pharm. Bull.* 39 (1991) 277–281. doi:10.1248/CPB.39.277.
- [25] D.J. Watkin, R.I. Cooper, Howard Flack and the Flack Parameter, *Chemistry (Easton).* 2 (2020) 796–804. doi:10.3390/CHEMISTRY2040052.
- [26] G. Poli, C. Granchi, F. Rizzolio, T. Tuccinardi, Application of MM-PBSA Methods in Virtual Screening, *Molecules.* 25 (2020) 1971. doi:10.3390/molecules25081971.

- [27] X.W. Luo, Y. Lin, Y.J. Lu, X.F. Zhou, Y.H. Liu, Peptides and polyketides isolated from the marine sponge-derived fungus *Aspergillus terreus* SCSIO 41008, *Chin. J. Nat. Med.* 17 (2019) 149–154. doi:10.1016/S1875-5364(19)30017-2.
- [28] G. Cazzaniga, M. Mori, L.R. Chiarelli, A. Gelain, F. Meneghetti, S. Villa, Natural products against key *Mycobacterium tuberculosis* enzymatic targets: Emerging opportunities for drug discovery, *Eur. J. Med. Chem.* 224 (2021) 113732. doi:10.1016/J.EJMECH.2021.113732.
- [29] G. Wolber, T. Langer, LigandScout: 3-D Pharmacophores Derived from Protein-Bound Ligands and Their Use as Virtual Screening Filters, *J. Chem. Inf. Model.* 45 (2005) 160–169. doi:10.1021/ci049885e.
- [30] G. Poli, T. Seidel, T. Langer, Conformational Sampling of Small Molecules With iCon: Performance Assessment in Comparison With OMEGA, *Front. Chem.* 6 (2018) 299. doi:10.3389/fchem.2018.00229.
- [31] J.D. Durrant, J.A. McCammon, BINANA: A novel algorithm for ligand-binding characterization, *J. Mol. Graph. Model.* 29 (2011) 888–893. doi:10.1016/j.jmgm.2011.01.004.
- [32] G. Poli, M. Lapillo, V. Jha, N. Mouawad, I. Caligiuri, M. Macchia, F. Minutolo, F. Rizzolio, T. Tuccinardi, C. Granchi, Computationally driven discovery of phenyl(piperazin-1-yl)methanone derivatives as reversible monoacylglycerol lipase (MAGL) inhibitors, *J. Enzyme Inhib. Med. Chem.* 34 (2019) 589–596. doi:10.1080/14756366.2019.1571271.
- [33] G. Poli, M. Lapillo, C. Granchi, J. Caciolla, N. Mouawad, I. Caligiuri, F. Rizzolio, T. Langer, F. Minutolo, T. Tuccinardi, Binding investigation and preliminary optimisation of the 3-amino-1,2,4-triazin-5(2H)-one core for the development of new Fyn inhibitors, *J. Enzyme Inhib. Med. Chem.* 33 (2018) 956–961. doi:10.1080/14756366.2018.1469017.
- [34] O.H. Lowry, N.J. Rosebrough, A.L. Farr, R.J. Randall, Protein measurement with the Folin

phenol reagent, *J. Biol. Chem.* 193 (1951) 265–275.

- [35] M.C. Burla, R. Caliandro, B. Carrozzini, G.L. Cascarano, C. Cuocci, C. Giacovazzo, M. Mallamo, A. Mazzone, G. Polidori, Crystal structure determination and refinement via SIR2014, *J. Appl. Crystallogr.* 48 (2015) 306–309. doi:10.1107/S1600576715001132.
- [36] G.M. Sheldrick, Crystal structure refinement with SHELXL, *Acta Crystallogr. Sect. C Struct. Chem.* 71 (2015) 3–8. doi:10.1107/S2053229614024218.
- [37] M. Nardelli, PARST 95 – an update to PARST : a system of Fortran routines for calculating molecular structure parameters from the results of crystal structure analyses , *J. Appl. Crystallogr.* 28 (1995) 659–659. doi:10.1107/s0021889895007138.
- [38] I.J. Bruno, J.C. Cole, M. Kessler, J. Luo, W.D.S. Motherwell, L.H. Purkis, B.R. Smith, R. Taylor, R.I. Cooper, S.E. Harris, A.G. Orpen, Retrieval of Crystallographically-Derived Molecular Geometry Information, *J. Chem. Inf. Comput. Sci.* 44 (2004) 2133–2144. doi:10.1021/CI049780B.
- [39] C.F. MacRae, I. Sovago, S.J. Cottrell, P.T.A. Galek, P. McCabe, E. Pidcock, M. Platings, G.P. Shields, J.S. Stevens, M. Towler, P.A. Wood, Mercury 4.0: From visualization to analysis, design and prediction, *J. Appl. Crystallogr.* 53 (2020) 226–235. doi:10.1107/S1600576719014092.
- [40] M.J. Turner, J.J. McKinnon, S.K. Wolff, D.J. Grimwood, P.R. Spackman, D. Jayatilaka, M.A. Spackman, *CrystalExplorer17*, (2017).
- [41] L.R. Chiarelli, M. Mori, G. Beretta, A. Gelain, E. Pini, J.C. Sammartino, G. Stelitano, D. Barlocco, L. Costantino, M. Lapillo, G. Poli, I. Caligiuri, F. Rizzolio, M. Bellinzoni, T. Tuccinardi, S. Villa, F. Meneghetti, New insight into structure-activity of furan-based salicylate synthase (MbtI) inhibitors as potential antitubercular agents, *J. Enzyme Inhib. Med. Chem.* 34 (2019) 823–828. doi:10.1080/14756366.2019.1589462.

